Electrocatalytic conversion of glycerol to oxalate on Ni oxide nanoparticles on oxidized multi-walled carbon nanotubes

Dulce M. Morales,[a,,†,‡] Daliborka Jambrec,[a,‡] Mariya A. Kazakova,[b] Michael Braun,[c] Nivedita Sikdar,[a] Adarsh Koul,[a] Ann Cathrin Brix,[a] Sabine Seisel,[a] Corina Andronescu,[c] and Wolfgang Schuhmann [a,*]*

a. Analytical Chemistry – Center of Electrochemical Sciences (CES), Faculty of Chemistry and Biochemistry, Ruhr University Bochum, Universitätsstr. 150, D-44780 Bochum, Germany

E-mail: wolfgang.schuhmann@rub.de; dulce.morales_hernandez@helmholtz-berlin.de.

b. Boreskov Institute of Catalysis, SB RAS, Lavrentieva 5, 630090 Novosibirsk, Russia

c. Chemical Technology III, Faculty of Chemistry and CENIDE Center for Nanointegration, University of Duisburg-Essen, University of Duisburg-Essen, Carl-Benz-Straße 199, 47057 Duisburg Germany

KEYWORDS: glycerol oxidation; nickel oxide; multi-walled carbon nanotubes; hydrogen production; value-added chemicals; oxalic acid.

ABSTRACT: Electrocatalytic oxidation of glycerol (GOR) as anode reaction in water electrolysis facilitates the production of hydrogen at the cathode at a substantially lower cell voltage compared to the oxygen evolution reaction. It simultaneously provides the basis for the production of value-added compounds at the anode. We investigate earth-abundant transition metal oxide nanoparticles (Fe, Ni, Mn, Co) embedded in multi-walled carbon nanotubes as GOR catalysts. Out of the four investigated composites, the Ni-based catalyst exhibits the highest catalytic activity towards the GOR according to rotating disk electrode voltammetry, reaching a current density of 10 mA cm^{-2} already at 1.31 V vs RHE, a potential below the formation of Ni^{3+}. Chronoamperometry conducted in a flow-through cell followed by HPLC analysis is used to identify and quantify the GOR products over time, revealing that the applied potential, electrolyte concentration and duration of the experiment impact strongly the composition of the products mixture. Upon optimization, the GOR is directed towards oxalate production. Moreover, oxalate is not further converted and hence accumulates as a major organic product under the chosen conditions in a concentration ratio of 60:1 with acetate as minor product after 48 h electrolysis in 7 M KOH, which represents a promising route for the synthesis of this highly valued product.

INTRODUCTION

Water electrolysis is regarded as one of the most promising routes towards sustainable energy conversion and storage. It enables the utilization of renewable energy for the production of hydrogen without generating greenhouse gases or any other pollutant. Yet, the use of water electrolyzers on a large scale remains challenging due to their low efficiencies in comparison to fossil fuel-based technologies. This is partly due to the high energy input required by the anodic process, namely, the oxygen evolution reaction (OER), as well as to the expensiveness and scarcity of precious metal-based catalytic materials commonly employed to drive this reaction.[1,2]

Approaches to mitigate the high costs related to the OER involve using low-cost, earth-abundant oxygen-evolving catalysts,[3–6] the integration of an alternative anode reaction that requires comparatively lower overpotentials to replace the OER,[7–9] or both.[10–12] In addition to this, by using an alternative oxidative electrosynthesis reaction, the possibility of valorization of anode products–along with the production of hydrogen or carbon-based fuels at the cathode–is enabled.[13–18] An example of such a reaction is the electrocatalytic oxidation of glycerol (GOR). As the global production of biodiesel increases in which glycerol is a byproduct,[19] glycerol is presently regarded as a treasure for electrocatalysis with the potential of leading to the formation of a wide variety of products upon its oxidation (**Scheme S1**).[20,21] One of the GOR products of highest interest is oxalic acid due to its diverse applications, for instance, in the cosmetics industry as a component in skin care exfoliating agents,[21] as a building block in polymer synthesis,[22] as a bleaching agent, and several others.[23] Thus, new methods and technologies for oxalic acid production are rising, some involving electrosynthesis routes.[22,23] Hence, the electrochemical synthesis of oxalic acid *via* the GOR is of great interest for potential industrial applications. Nevertheless, a significant challenge is the control of the GOR selectivity while simultaneously achieving high reaction rates and high conversions[24,25] since its various reaction pathways often lead to complex mixtures as the final product.[20,21,26] There is currently a limited number of studies reporting highly active GOR catalysts based on earth-abundant materials,[27–31] and even less demonstrating high selectivity towards value-added products. Among them, Ni-based catalysts seem to be promising candidates in terms of catalytic GOR performance, offering relatively low overpotentials and predominant selectivity towards formate.[27,28,32] While some studies demonstrate the formation of C2 or C3 products, improved selectivity still represents a major challenge.[33–35]

We investigate earth-abundant metal oxide nanoparticles (CoO_x, FeO_x, MnO_x, NiO_x) embedded on oxygen-functionalized multi-walled carbon nanotubes (MWCNTs-Ox) as electrocatalytic materials for the GOR by rotating disk electrode (RDE) voltammetry. The stability of the catalyst with the highest GOR activity, namely, NiO_x/MWCNTs-Ox, and its selectivity towards the formation of value-added products are evaluated using a two-compartment flow-through electrolyzer. We successfully obtained oxalic acid as the predominant product upon optimization of the applied potential, the electrolyte concentration, and the experiment's duration, which all impact strongly on the product distribution.

RESULTS AND DISCUSSION

The purpose of substituting the OER by an alternative anode process, specifically the GOR, is twofold: on the one hand, as the GOR needs lower overpotentials than the OER, the overall cell voltage required for electrolysis is decreased, resulting in a lower energy cost for the coupled hydrogen production. On the other hand, the GOR offers the possibility of generating products with a value higher than that of oxygen. These two objectives will be discussed separately in the following two subsections.

MO_x/MWCNTs-Ox as catalyst for the GOR as alternative anode reaction for water electrolysis

The investigated catalysts are multi-phase transition metal oxide nanoparticles embedded in oxygen-functionalized multi-walled carbon nanotubes (MWCNTs-Ox), and are hereafter denoted as MO_x/MWCNTs-Ox, with M = Co, Fe, Mn, or Ni. Corresponding high-resolution TEM micrographs are shown in **Figure S1**. Synthesis and in-depth characterization of these materials were reported previously,[36–39] and are summarized in **Table S1**. Additionally, corresponding

TEM micrographs, XRD patterns and XPS spectra are shown in **Figures S1**, **S2** and **S3**, respectively. The catalytic activity of the MO_x/MWCNTs-Ox catalysts towards the OER was investigated by rotating disk electrode (RDE) voltammetry in 1 M KOH as electrolyte. The corresponding polarization curves (**Figure 1,** full lines) show reproducible voltammetric responses with an activity trend in terms of current density and overpotential in the order Ni > Co > Fe > Mn, in agreement with previous reports on metal oxide-based catalyst for alkaline OER.[40,41] The potentials required to reach a current density of 10 mA cm^{-2} (E_{OER}) were determined for each catalyst (**Table 1**). Out of the four catalysts, NiO_x/MWCNTs-Ox is the most active catalyst with an E_{OER} value of 1.59 V vs RHE, which is about 30, 50 and 110 mV lower than those of the Co, Fe and Mn analogs, respectively.

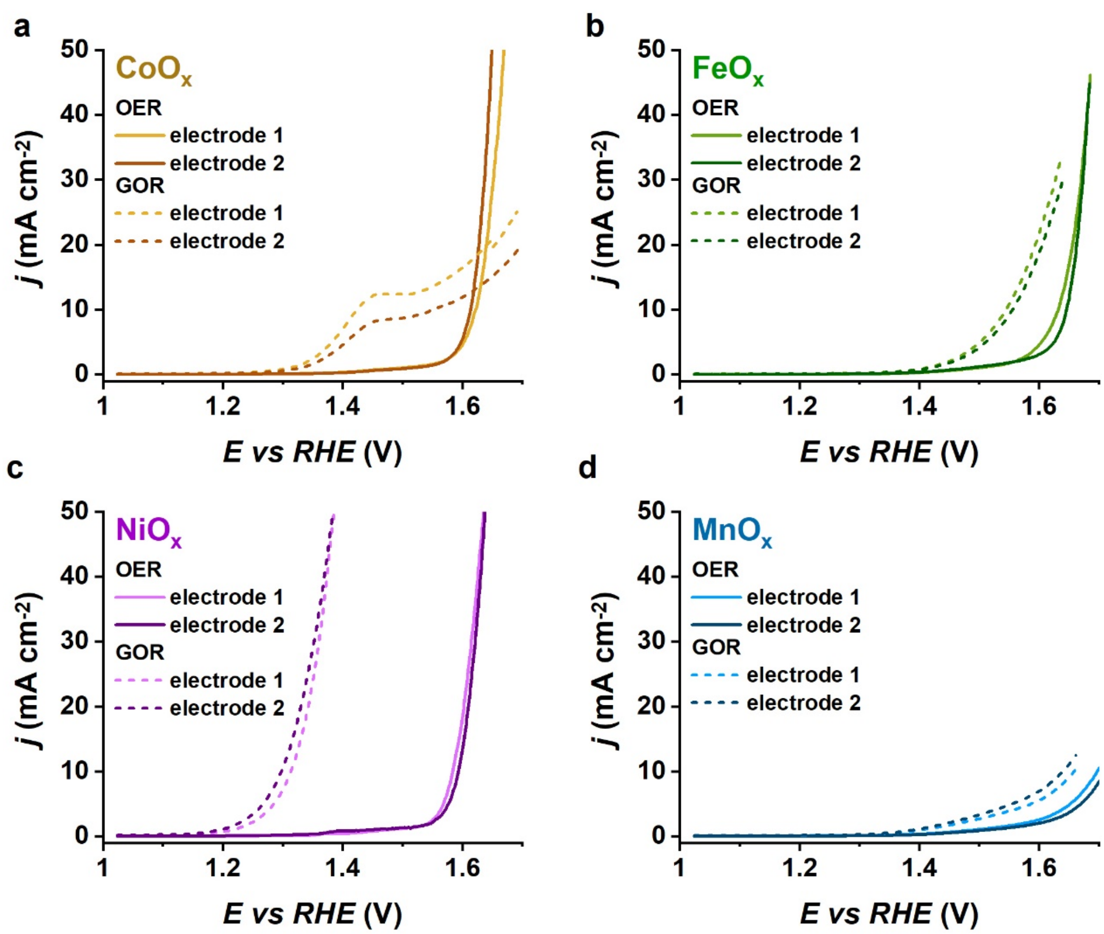

Figure 1. Linear sweep voltammograms of MO_x/MWCNTs-Ox with M = (a) Co, (b) Fe, (c) Ni, and (d) Mn, recorded at a scan rate of 5 mV s^{-1} and an electrode rotation of 1600 rpm in Ar-saturated 1 M KOH solution in the presence (dashed lines) or absence (full lines) of 1 M glycerol, corresponding to the GOR and the OER, respectively. All measurements were done in duplicate, with electrode 1 and 2 being two independent, freshly prepared catalyst-modified electrodes. The four plots are displayed with the same scale to facilitate their comparison.

Table 1. Activity parameters of MO_x/MWCNTs-Ox catalysts.

Sample	E_{OER} [(a)] (V vs RHE)	E_{GOR} [(b)] (V vs RHE)	$\Delta\eta_{anode}$ [(c)] (mV)
CoO_x/MWCNTs-Ox	1.62	1.49	130
FeO_x/MWCNTs-Ox	1.64	1.55	90
NiO_x/MWCNTs-Ox	1.59	1.31	280
MnO_x/MWCNTs-Ox	1.70	1.66	40

[(a)] E vs RHE at 10 mA cm^{-2} during the OER; [(b)] E vs RHE at 10 mA cm^{-2} during the GOR; [(c)] E_{OER}-E_{GOR}

Similarly, linear sweep voltammograms were obtained for each catalyst upon addition of 1 M glycerol to the 1 M KOH electrolyte. As shown in **Figure 1** (dotted lines), the activity trend for the OER was maintained in the order Ni > Co > Fe > Mn for the GOR. The potentials required to reach a current density of 10 mA cm^{-2} in the presence of glycerol (E_{GOR}) (**Table 1**) were lower than the corresponding E_{OER}. The difference between the E_{OER} and E_{GOR}, denoted here as $\Delta\eta_{anode}$ (**Table 1**), represents a measure of the saved energy by replacing the OER with the GOR at a current density of 10 mA cm^{-2}. The catalyst exhibiting the lowest E_{GOR} and the largest $\Delta\eta_{anode}$ is

NiO_x/MWCNTs-Ox, with an E_{GOR} = 1.31 V vs RHE and a $\Delta\eta_{anode}$ = 280 mV. CoO_x/MWCNTs-Ox exhibits the second-largest $\Delta\eta_{anode}$ value; however, the GOR current densities are substantially lower. MnO_x/MWCNTs-Ox shows the highest E_{OER} and E_{GOR} values, and the lowest $\Delta\eta_{anode}$ value.

One of the main advantages of the chosen catalyst synthesis route is that it effectively leads to MO_x/MWCNTs-Ox materials with controlled structural properties.[42,43] The total metal loading and the specific surface area (*SSA*) are similar for the four catalysts, ranging from 13.4 to 13.8 wt.% and 244 to 262 m^2 g^{-1}, respectively (**Table S1**).[36–38] To confirm that the surface area differences do not impact substantially the observed activity trends, double layer capacitance (C_{DL}), which is proportional to the electrochemically active surface area, was determined for each of the samples by scan rate-dependent cyclic voltammetry following a recently reported procedure[44] exemplified in **Figure S4**. The obtained results, summarized in **Table S2**, were compared to the activity parameters E_{OER} and E_{GOR}, as well as to their corresponding *SSA* in **Figure S5**, showing no clear correlation between activity and C_{DL} or *SSA*, and suggesting that the intrinsic activity has a stronger impact than the differences in (electrochemical) surface area. MO_x/MWCNTs-Ox are thus convenient material systems for a comparative evaluation of the intrinsic catalytic properties of oxide nanoparticles of different earth-abundant metals. Furthermore, the often experienced electrical conductivity limitations inherent to metal oxides are overcome mainly by using MWCNTs-Ox as support material.[45,46] However, it is important to note that contributions to the measured OER and GOR currents due to the catalytic activity of the MWCNTs-Ox support cannot be entirely excluded (**Figure S6**). In addition to this, NiO_x/MWCNTs-Ox displays a higher dispersion of oxide nanoparticles, as well as a similar particle size (~5 nm) and distribution of particles located inside and outside the channels of the

MWCNTs-Ox (**Table S1**), which may contribute to the considerably larger catalytic activity of the Ni-containing sample as compared to MO_x/MWCNTs-Ox with M=Mn, Fe or Co. Yet, another important difference is the type of bulk phase, which according to XRD was consisted of NaCl-type Ni (oxidation state 2+)[37] and spinel-type oxide in the cases of Fe, Mn, or Co.[36,39] The higher content of M^{2+} in NiO_x/MWCNTs-Ox could facilitate substrate adsorption in which the glycerol molecules are adsorbed onto NiO and/or $Ni(OH)_2$, rather than onto NiOOH species.[47] This becomes obvious from the linear sweep voltammograms in the absence, and in the presence of either glycerol or ethanol, corresponding to the OER, the GOR and the ethanol oxidation reaction (EOR), respectively (**Figure 2**). In the absence of the alcohols, the redox feature corresponding to the $Ni^{2+} \rightarrow Ni^{3+}$ transition is visible in the potential range from 1.35 to 1.4 V vs RHE. In the case of the EOR, however, the Ni oxidation disappears since the EOR is initiated with the oxidation of Ni^{2+}, in agreement with previous reports on electrocatalytic oxidation of methanol and ethanol on nickel-based catalysts.[48–50] The overpotential of the GOR, however, was observed at considerably lower potentials than that for the oxidation of Ni^{2+}, suggesting that the reaction can occur without the formation of NiOOH species. Such "early GOR onsets" have been observed with other Ni^{2+}- catalyst,[27,28,32] and may be due to mechanistic differences between oxidation of monohydric and polyhydric alcohols, involving different transition states and/or different catalytic sites.[51] Thus, the GOR potential relative to the $Ni^{3+/2+}$ peak determines the nature of the active sites in NiO_x/MWCNTs-Ox and, likely, the selectivity of the GOR. The effect of the applied potential on the product distribution during the GOR was therefore investigated.

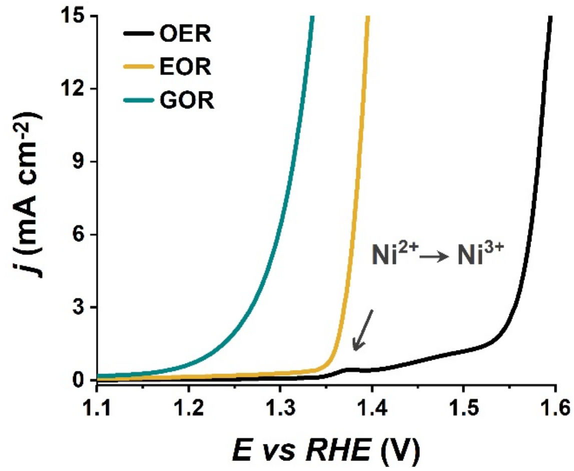

Figure 2. Linear sweep voltammograms obtained with NiO_x/MWCNTs-Ox at 5 mV s^{-1} scan rate and 1600 rpm electrode rotation in Ar-saturated 1 M KOH solution in the absence (OER), or presence of 1 M ethanol (EOR) or 1 M glycerol (GOR).

GOR selectivity of NiO_x/MWCNTs-Ox

NiO_x/MWCNTs-Ox exhibited the highest activity towards the GOR, rendering it an attractive candidate for further investigation of its selectivity. Chronoamperometric measurements were conducted in a flow-through electrolyzer, where the anode and cathode compartments were separated by an anion-exchange membrane (**Figure 3a**). 1 M KOH solutions with and without 100 mM glycerol were pumped from their respective reservoirs to the anode and cathode compartments, respectively, and recirculated throughout the entire duration of the measurement, while a constant potential was applied to the anode. At certain time intervals, samples of the electrolyte were taken from the anode compartment and immediately acidified for subsequent HPLC analysis to monitor the concentration of glycerol ($C_{glycerol}$) and GOR products.

In a first experiment, a constant potential of 1.41 V vs RHE was applied for 72 h with the purpose of establishing whether NiO_x/MWCNTs-Ox is sufficiently stable to allow for the investigation of the GOR selectivity. **Figures 3b** and **3c** show the current densities recorded during chronoamperometry and the $C_{glycerol}$ determined by HPLC, respectively, as a function of electrolysis time. During the first 24 h (cycle 1), the apparent decrease of the current density correlates with a decrease in $C_{glycerol}$. To confirm that the decrease is due to glycerol consumption rather than the loss or deactivation of the catalyst, after cycle 1, a fresh aliquot of 1 M glycerol dissolved in 1 M KOH solution was added into the reservoir to reestablish the initial $C_{glycerol}$ (100 mM). A full recovery of the initial current density was obtained as shown in **Figure 3b**. During 24 and 48 h (cycle 2), both the current density and the $C_{glycerol}$ decreased similarly as during cycle 1. At the end of cycle 2 the procedure was repeated, exhibiting a similar behavior between 48 and 72 h (cycle 3). The reproducibility of the recorded current densities indicates that NiO_x/MWCNTs-Ox is stable at the selected operating conditions.

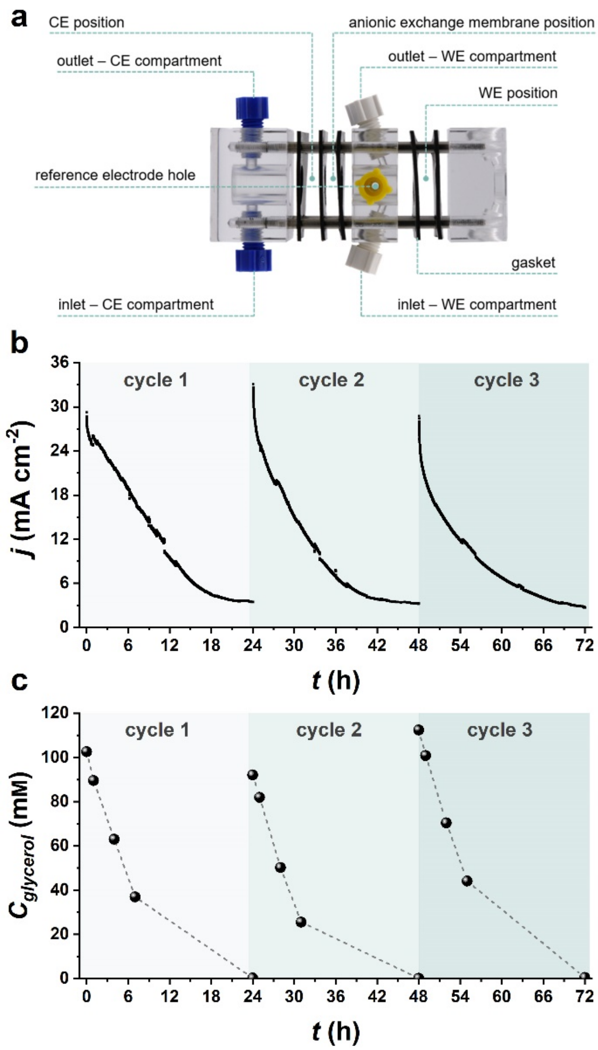

Figure 3. (a) Two-compartment flow-through cell used for selectivity evaluation of the GOR at NiO_x/MWCNTs-Ox. (b) Chronoamperometry at 1.41 V vs RHE for 72 h in glycerol-containing 1 M KOH as electrolyte for the anode compartment. The initial glycerol concentration was 100 mM; an aliquot of 1 M glycerol/1 M KOH solution was injected after 24 and again after 48 h to reestablish the initial glycerol concentration. (c) Glycerol concentration ($C_{glycerol}$) as a function of time showing three cycles of complete conversion in 24 h intervals. Dashed lines in (c) are guide for the eye.

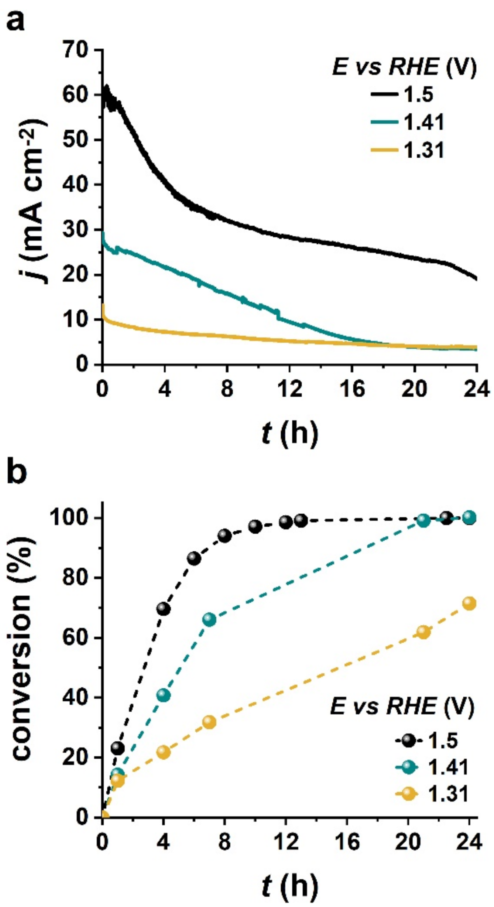

Figure 4. (a) Chronoamperograms recorded with NiO_x/MWCNTs-Ox at 1.5, 1.41 and 1.31 V vs RHE in 1 M KOH solution with an initial glycerol concentration of 100 mM, and the corresponding (b) conversion of glycerol monitored over 24 h. Dashed lines in (b) are guides for the eye.

Chronoamperometry was performed for 24 h at three different potentials, namely 1.31, 1.41 and 1.5 V vs RHE to investigate the product distribution in dependence on the applied potential (**Figure 4a**). Note that the lowest applied potential is less anodic than that of the $Ni^{2+} \rightarrow Ni^{3+}$ oxidation (**Figure 2**). Product identification and quantification were made by HPLC, and a representative chromatogram is shown in **Figure S7**. Oxygen from the competing OER and carbonate are expected side-products; however, they were not detected by HPLC and are not considered in the following discussion. The conversion of glycerol during electrolysis is shown as a function of time in **Figure 4b**. As expected, at a higher potential not only higher currents were obtained but also a higher glycerol conversion rate. Full conversion was attained after 12 h with 1.5 V vs RHE, while nearly 24 h were required when the GOR was performed at 1.41 V vs RHE, and for 1.31 V vs RHE only about 70% conversion was achieved after 24 h.

$C_{glycerol}$ and the concentrations of the identified products are shown as a function of time in **Figure 5**. Faradaic efficiency (*%FE*) profiles corresponding to the individual identified products formed at the three potentials are shown in **Figures S8a**, **S8b** and **S8c**. It is important to note that the GOR products were detected in the form of organic acids due to sample treatment prior to HPLC, however, the compounds formed during electrolysis are the corresponding bases due to the high pH value of the electrolyte. For instance, if formate was generated during the reaction, it was detected in the form of formic acid. In the following, formed products and detected compounds are differentiated by using the appropriate form. For 1.31, 1.41 and 1.5 V vs RHE, formic acid was detected as the main product (**Figure 5a**, **5c**, **5e**), while the concentrations of other minor products did not exceed 8 mM (**Figure 5b**, **5d**, **5f**). During the first hours of electrolysis at 1.5 V vs RHE, the concentration of formic acid (C_{FA}) increased along with the depletion of glycerol (**Figure 5a**); however, after a significant amount of glycerol was oxidized, a decrease in C_{FA} started, indicating that formate converts to carbonate. This can be also visualized in **Figure S8c**, where the *%FE* profile corresponding to formate decreases from 66% during the first hour to 50% after 4 h, but more rapidly afterwards. Evidently, glycerol adsorbs preferentially at the active sites of the catalyst, hindering thus the oxidation of formate until glycerol is sufficiently depleted. Minor detected products included oxalic acid and traces of glycolic, glyceric, acetic, lactic, and tartronic acid (**Figure 5b**). The oxalic and glycolic acid concentration profiles exhibited an initial increase followed by a decrease after longer electrolysis times, suggesting that oxalate and glycolate are susceptible to be oxidized upon depletion of other compounds that are adsorbed more easily.

At 1.41 V vs RHE (**Figure 5c**), $C_{glycerol}$ and C_{FA} displayed profiles similar to those at 1.5 V vs RHE (**Figure 5a**), but at a lower rate. Additionally, higher *%FEs* towards the formation of formate were observed throughout the measurement at 1.41 V vs RHE compared to those obtained at 1.5 V vs RHE, indicating a lower carbonate yield (**Figures S8b** and **S8c**). Traces of glycolic, oxalic, acetic, lactic and glyceric acid were identified as minor products (**Figure 5d**). While the concentration profiles of glycolic acid (C_{GA}) obtained at the two potentials were similar, the concentration of oxalic acid (C_{OA}) was considerably lower in the case of electrolysis conducted at 1.41 V vs RHE. Moreover, at 1.5 V vs RHE, oxalic acid was detected already during the first 60 min. In comparison, the concentration profiles observed at 1.41 V vs RHE indicate that oxalate was formed only when depletion of glycolate started. This suggests that oxalate is formed by the oxidation of glycolate at this potential.

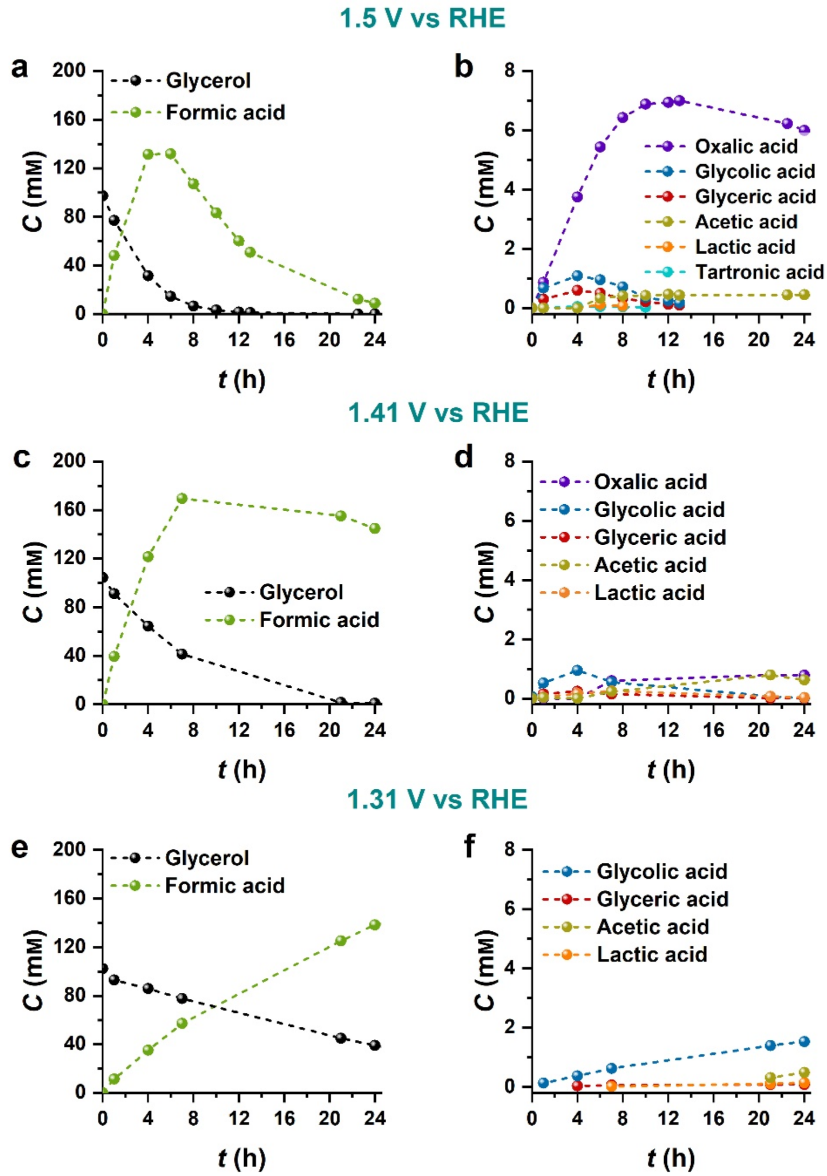

Figure 5. Concentration of glycerol and GOR products as a function of time during electrolysis catalyzed by NiO_x/MWCNT-Ox. Electrolyte samples were collected during chronoamperometry measurements at (a,b) 1.5 V, (c,d) 1.41 V, and (e,f) 1.31 V vs RHE. The initial electrolyte composition was 100 mM glycerol dissolved in 1 M KOH solution. For better visibility, minor products are presented separately. Dashed lines are guides to the eye.

At 1.31 V vs RHE, production of formate dominated throughout the full experiment, observing a *%FE* of 96% during the first 60 min, and retaining an efficiency of 67% after 24 h (**Figure**

S8a). The minor identified products were glycolic acid, and traces of glyceric, lactic and acetic acid. Within the time frame of the experiment, no decrease in C_{GA} was observed, suggesting that glycolate did not oxidize further to oxalate under these conditions, likely due to the considerably lower driving force. Earlier, we speculated that performing electrolysis at a potential less anodic than that of the formation of Ni^{3+} species could result in a modulation in selectivity. The low conversion of glycerol, however, resulted in a low yield of minor products, which makes it difficult to distinguish between a change in selectivity and a change in product distribution due to the low driving force.

Given that for all the three investigated potentials the main product obtained with NiO_x/MWCNTs-Ox was formate, it is preferable to apply the highest of them, on the one hand, to achieve complete conversion of glycerol in a shorter time, and on the other, to achieve higher current densities, thus favoring the production of hydrogen at the cathode. Considering that industrial alkaline electrolyzers operate at KOH concentrations in the range from 25 to 30 wt.%,[52] we investigated the GOR driven on NiO_x/MWCNTs-Ox in 7 M KOH as electrolyte. **Figure 6a** shows a comparison of RDE voltammograms recorded in the presence of glycerol (1 M) dissolved in either 1 M (black) or 7 M (teal) KOH. The activity of NiO_x/MWCNTs-Ox was considerably larger in the more concentrated electrolyte. The E_{GOR} value in 7 M KOH solution was by about 40 mV lower than the E_{GOR} in 1 M KOH, rendering NiO_x/MWCNTs-Ox-driven GOR a promising alternative anode reaction in hydrogen production in highly concentrated electrolytes.

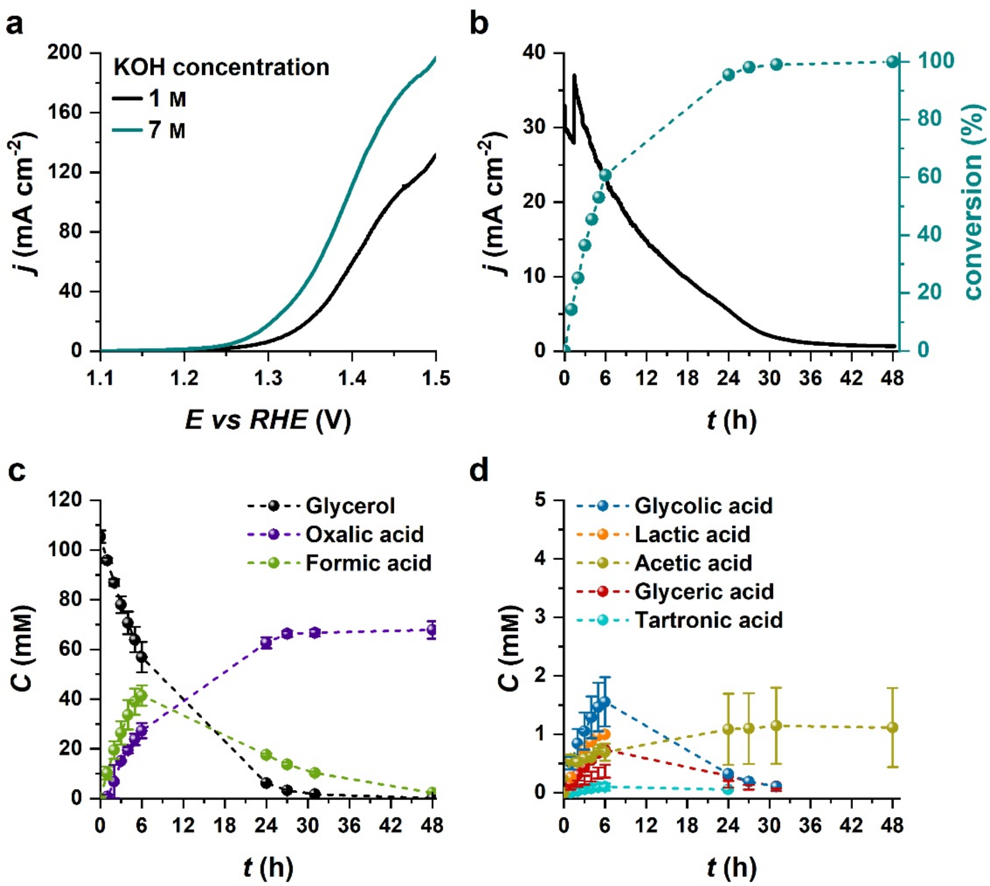

Figure 6. (a) Comparison of NiO_x/MWCNTs-Ox-catalyzed GOR in Ar-saturated 1 M and 7 M KOH solution containing glycerol. RDE voltammograms were recorded at 5 mV s^{-1} scan rate and 1600 rpm electrode rotation. The initial glycerol concentration was 1 M. (b) Chronoamperogram recorded at 1.5 V vs RHE in 7 M KOH with an initial glycerol concentration of 100 mM using a two-compartment flow-through cell, and the corresponding conversion of glycerol determined by HPLC analysis. (c) Concentrations of glycerol, main GOR products, and (d) minor products of samples collected throughout 48 h NiO_x/MWCNTs-Ox-catalyzed electrolysis conducted at 1.5 V vs RHE in 7 M KOH containing initially 100 mM glycerol. Error bars represent the standard deviation from two independent measurements. Dashed lines are guides to the eye.

The impact of the KOH concentration on the GOR selectivity of NiO_x/MWCNTs-Ox was investigated by chronoamperometry using the flow-through cell (**Figure 3a**) and a 7 M KOH solution containing an initial $C_{glycerol}$ of 100 mM. The chronoamperograms and the conversion of glycerol as a function of time are shown in **Figure 6b**. The concentration profiles of the major and minor products are shown in **Figure 6c** and **Figure 6d**, respectively. Corresponding *%FE* profiles are shown in **Figure S8d**. Interestingly, during the first 6 h, the main identified products, namely formic and oxalic acid, were found in comparable concentrations, which differed substantially from the product profile observed in 1 M KOH at the same potential, where C_{FA} was about 25 times larger than C_{OA}. Likely, formate undergoes faster oxidation in 7 M KOH than in 1 M KOH, thus contributing more substantially to the measured currents. Furthermore, after 7 h electrolysis, *%FE* corresponding to the formation of oxalate (34%) was nearly twice that of formate (18%) (**Figure S8d**).

At longer electrolysis times, while C_{FA} continuously decreased, the C_{OA} increased continuously until reaching ~70 mM after about 30 h, corresponding to a 99 % conversion of glycerol. After this time, the C_{OA} concentration remained constant, while C_{FA} decreased further. This final period shows that oxalate does not oxidize further at these particular experimental conditions, and that the product distribution depends strongly on the duration of the experiment. In other words, while a mixture of formate and oxalate was obtained during the first hours of the measurement, maintaining the reaction conditions for a longer time allowed to oxidize formate, thus obtaining oxalate with substantially higher purity. We consider this as one of our most important findings, since, by carefully selecting the electrolysis conditions, it is possible to mainly obtain a single value-added product, i.e. oxalate, however to the expense that part of the energy is consumed for the total oxidation of glycerol to CO_2.

The minor products included glycolic, lactic, acetic, glyceric and tartronic acid (**Figure 6d**). The majority of these products exhibited concentration profiles similar to that of formic acid: the maximum concentration (below ~2 mM in all cases) was reached at about 6 h and decreased subsequently until complete oxidation at about 32 h. Only acetic acid was preserved over the 48-h measurement, displaying a concentration profile similar to that of oxalic acid. By the end of the measurement, the only compounds in the solution were oxalic and acetic acid in a concentration ratio of 60:1. The composition of the product mixture after 48 h electrolysis was further investigated by ^{13}C NMR. As shown in **Figure S9**, the signals at 164 and 168 ppm correspond to oxalate[53] and potassium carbonate, respectively. No other compound, including acetic acid due to its low concentration, could be detected by ^{13}C NMR, confirming that oxalate was the main product. Furthermore, **Figure S10** shows XRD patterns of carbon paper-supported NiO_x/MWCNTs-Ox before and after 24 h electrolysis in 1 M and 7 M KOH in the presence of 100 mM glycerol. After conducting the GOR in 1 M KOH, potassium carbonate and bicarbonate could be detected in the catalyst sample along with some traces of nickel bicarbonate (pdf: 00-012-0292, 00-012-0276, 00-015-0782, 01-075-5384), whereas by performing the reaction in 7 M KOH, even stronger peaks of the different carbonates could be observed. Additionally, the diffraction pattern of nickel hydroxide and potassium hydrogen oxalate have been found (pdf: 00-014-0117, 00-014-0810, 00-029-0868). These results show a promising electrocatalytic synthesis route of oxalate from glycerol using NiO_x/MWCNTs-Ox as electrocatalyst in a highly alkaline electrolyte.

CONCLUSION

Earth-abundant transition metal oxide nanoparticles (Fe, Ni, Mn and Co) embedded in oxygen-functionalized multi-walled carbon nanotubes were investigated as catalysts for the OER and GOR in alkaline media. The GOR was achieved at lower potentials than the OER, rendering the GOR an attractive alternative to the OER as anode reaction in water electrolysis. Particularly, the Ni-based catalyst displayed high activity towards the GOR, reaching a current density of 10 mA cm^{-2} at 1.31 V vs RHE, a potential below Ni^{2+} to Ni^{3+}, oxidation indicating that the GOR can be driven by catalytic sites different than NiOOH. In contrast, the OER or the oxidation of ethanol require Ni^{3+} species to be formed prior to electrocatalysis. Chronoamperometric measurements in a two-compartment flow-through cell at 1.31, 1.41 and 1.5 V vs RHE in 1 M KOH with an initial glycerol concentration of 100 mM allow, firstly, identifying GOR products, and secondly, monitoring their concentrations as a function of electrolysis time. Increasing the KOH concentration to 7 M, a concentration typically used in industrial water electrolyzers, led to a further decrease of the GOR overpotentials along with a substantial difference in the product distribution, yielding a mixture of formate and oxalate as the main products during the first 6 h. After this time, formate and all minor products underwent oxidation, while oxalate remained stable. After 48 h electrolysis, the only remaining products were oxalic and acetic acid in a concentration ratio of 60:1. Hence, and despite a relatively low Faradaic efficiency, conducting the GOR on multi-walled carbon nanotubes-supported Ni oxide nanoparticles did not only benefit in terms of energy consumption from the lower overpotentials in comparison to the OER, but also in terms of overall cost, as the formation of hydrogen is subsidized by the value of the purified oxalate. These results pave the way to using the GOR as a promising alternative anode reaction in water electrolysis, offering the possibility of concomitantly synthesizing a value-added chemical, namely, oxalate.

EXPERIMENTAL

Catalyst synthesis and characterization: Synthesis of monometallic Fe, Co, Ni and Mn-based catalysts was performed following a procedure reported previously.[36] Firstly, multi-walled carbon nanotubes (MWCNTs) were grown by chemical vapor deposition of ethylene at 680 °C using Fe-Co/Al_2O_3 as growth catalyst.[54,55] The obtained material was treated in aqueous HCl solution (15 vol%) for 4 h to remove the majority of catalyst residues and washed with distilled water until neutral pH, obtaining thus MWCNTs with metal impurities in the order of ppm.[56] The dry MWCNTs were then treated in concentrated HNO_3 for 2 h, washed with distilled water until neutral pH to obtain oxygen-functionalized MWCNTs (MWCNTs-Ox).[43] Subsequently, the dry powder was subjected to incipient wet impregnation using as precursors aqueous solutions of either Ni(II), Co(II), Fe(III), or Mn(II) nitrates, followed by drying at 110 °C for 4 h, and annealing at 350 °C for 4 h. Metal oxide nanoparticles of the corresponding metal precursor embedded in MWCNTs-Ox, with a total metal loading of ~14 wt% were obtained. Characterization of the different catalysts was reported previously,[36,37,39] and is summarized in **Table S1**. Corresponding TEM micrographs, XRD patterns and XPS spectra are shown in **Figures S1**, **S2** and **S3**, respectively. Specific surface area measurements were conducted via N_2 adsorption isotherms obtained at a temperature of 77 K using an ASAP-2400 instrument (Micromeritics). Phase composition of samples before and after electrolysis was investigated by XRD performed with a theta-theta powder diffractometer (Bruker D8 Discover) equipped with a Cu-Kα radiation source (λ = 1.5418 Å). XRD patterns were recorded in the diffraction angle range between 20° and 80° using a step width of 0.02°. Carbon paper-supported samples were placed into a PMMA sample holder and transferred to the XRD instrument. DIFFRAC.EVA V5.0 software has been used for data extraction as well as $K\alpha_2$ and background correction.

Investigation of catalytic activity: The catalytic activity of the synthesized materials was investigated using rotating disk electrode (RDE) voltammetry conducted in a three-electrode configuration cell using an Autolab PGSTAT128N potentiostat (Metrohm) and a RDE 80793 rotator (Metrohm). A mixture of water, ethanol and as-purchased Nafion solution (5% in a mixture of alcohols) with a 49:49:2 volume ratio was used as dispersion media for 5 mg mL^{-1} catalyst subjected to sonication for 15 min. Pre-polished glassy carbon RDEs of 0.113 cm^2 geometric area were modified by drop-casting 4.8 μL ink and dried under air to achieve catalyst films with a loading of 210 μg cm^{-2}. The catalyst-modified RDEs, a double-junction Ag|AgCl|KCl (3 M) electrode filled with 1 M KOH solution in the outer compartment, and a Pt mesh were used as the working, reference and counter electrodes, respectively. The counter electrode was kept in a compartment separated by a glass frit during the measurements to avoid Pt contamination. Argon-saturated KOH solutions (1 or 7 M) in the absence or the presence of 1 M of either glycerol or ethanol were used as the electrolyte for the oxygen evolution, glycerol oxidation or ethanol oxidation reactions, respectively. Metal impurities contained in KOH solutions were removed using a Chelex cation-exchange resin[57] (Bio-Rad Laboratories) prior to measurements. Cyclic voltammograms were continuously collected at a scan rate of 100 mV s^{-1} in the potential ranges from -0.2 to 0.3 V vs Ag|AgCl|KCl (3 M) in the cases where ethanol or glycerol were present in the electrolyte, or from -0.2 to 0.5 V vs Ag|AgCl|KCl (3 M) in the cases where the alcohols were absent. Afterwards, electrochemical impedance spectroscopy (EIS) was conducted in the frequency range from 100 to 1 kHz with an amplitude of 10 mV (RMS) at open circuit potential to determine the uncompensated resistance (R_U) from the corresponding Nyquist plots. A linear sweep voltammogram was subsequently recorded in the potential range from 0.0 to 0.7 V vs Ag|AgCl|KCl (3 M) for the OER, or from 0.0 to 0.6 V vs Ag|AgCl|KCl (3 M) for GOR and EOR. All activity measurements were done in duplicate.

Determination of double layer capacitance: Scan rate-dependent voltammetry was conducted in Ar-saturated 1 M KOH solution for the determination of double layer capacitance (C_{DL}) of the four MO_x/MWCNTs-Ox samples according to a previously reported procedure.[44] In brief, cyclic voltammograms were collected in a 400 mV window in the non-faradaic potential region at scan rates of 0.1, 0.25, 0.5, 0.75, 1, 2.5 and 5 V s^{-1} until reproducible voltammograms were obtained. Charging currents (i_c) were extracted from the center potential from the last anodic and cathodic scans and plotted as a function of the scan rate (ν) and fitted to an allometric model to obtain C_{DL} and the exponent α according to **Equation 1**.

$$i_c = C_{DL} \cdot \nu^{\alpha} \quad (1)$$

Investigation of GOR selectivity: Chronoamperometric measurements were performed in a three-electrode configuration, two-compartment flow-through cell (**Figure 3a**) using a VP-300 potentiostat (BioLogic) controlled by the EC-Lab software. The Ni foam counter electrode was placed in the cathode compartment separated from the anode compartment employing a Fumasep FAA-3-PK-130 anionic exchange membrane (Fumatech). The working electrode (1 cm^2 exposed area) was prepared by dispersing 5 mg mL^{-1} NiO_x/MWCNTs-Ox powder in a mixture of ethanol and as-purchased Nafion solution (98:2 vol%) by sonication for 15 min, followed by drop-casting 1 mg cm^{-2} catalyst onto H23C2 carbon paper (Freudenberg) and drying at room temperature. A double-junction Ag|AgCl|KCl (3 M), containing 1 M KOH in the outer compartment was used as the reference electrode, and it was placed together with the working electrode in the anode compartment of the flow-through cell. Electrolytes were pumped through the anode and cathode compartments from independent reservoirs at a flow rate of 10.5 mL min^{-1} using a peristaltic pump. The anode reservoir contained 12 mL of a solution consisting of 100 mM glycerol dissolved in either 1 or 7 M KOH, while the cathode compartment contained the same volume of KOH at the corresponding concentration. Before the measurement, 10 cyclic voltammograms were recorded in the potential range from -0.2 to 0.4 V vs Ag|AgCl|KCl (3 M) at 100 mV s^{-1} scan rate. EIS was subsequently conducted in the frequency range from 100 to 1 kHz with an amplitude of 10 mV (RMS) at open circuit potential to determine R_U as described for the activity measurements. Afterwards, a linear sweep voltammogram was recorded in the range from 0 to 0.7 V vs Ag|AgCl|KCl (3 M) at 5 mV s^{-1} scan rate. Finally, the GOR was performed chronoamperometrically at constant potentials of 0.73, 0.5, or 0.35 V vs Ag|AgCl|KCl (3 M) for 24 or 48 h. During the measurement, samples of the electrolyte were collected at different time intervals and immediately acidified by adding diluted sulfuric acid for subsequent HPLC analysis.

Product analysis. Analyses of the obtained product mixtures were done using a Dionex ICS-5000+ HPLC (ThermoFisher) equipped with an Aminex HPX.87H ion-exclusion column and precolumn (Bio-Rad) using a refractive index (RI) detector (RefractoMax520) and a diode array detector (UV/VIS, Dionex UltiMate 3000). The measurements were performed at 70 °C and 0.6 mL min^{-1} flow rate, using 4 mM sulfuric acid as eluent. Sample preparation was done by filtering (0.2 µm pores) the collected acidified electrolyte. Calibration was performed using commercially available reference compounds in a concentration range from 0.1 to 100 mM in all cases except for formic acid and glycerol, for which the calibration was done in a concentration range from 0.1 to 1 M. Ammonium formate (Sigma-Aldrich, ≥ 99 %), sodium D-lactate (Aldrich, 99 %), glycolic acid (Sigma-Aldrich, 99 %), calcium L-(-)-glycerate dihydrate (Alfa Aesar), tartronic acid (Sigma-Aldrich, ≥ 97 %), oxalic acid (Fluorochem), and acetic acid (Sigma-Aldrich, 99.8 %) were used as received without further purification. All products were detected using the RI detector, except formic acid, which was quantified using the UV/VIS detector set at 220 nm, where glycerol is not detectable. Due to the overlapping of glycerol and formic acid peaks in the RI detector, the glycerol concentration was derived by subtracting the area of the formic acid peak that was calculated with the concentration detected by the UV/VIS detector considering the corresponding calibration factors (i.e. slopes of corresponding calibration curves).

^{13}C-NMR measurements were carried out using a Bruker Avance DRX-400 [SF (^{13}C): 100.62 MHz] with a ^{13}C with ^{1}H CPD decoupling pulse program, time per scan (*AQ*) of 0.6 s, relaxation delay (*D1*) of 2 s, number of scans (*NS*) of 32,000, and estimated total time of 24 h. Sample preparation was done by adding 120 µL D_2O to 480 µL electrolyte (20% dilution by D_2O). DMSO-D_6 was added as an internal standard.

Data processing: Potentials in the manuscript are reported with respect to the reversible hydrogen electrode (RHE) calculated according to **Equation 2**. The pH value of the electrolyte was determined according to **Equation 3,** considering activity coefficient values (γ) of 0.766 [58,59] and 1.298 [60] for 1 and 7 M KOH solutions, respectively.

$$E_{RHE} = E_{Ag|AgCl|KCl} + E^{0}_{Ag|AgCl|KCl} + 0.059 \cdot \mathrm{pH} \qquad (2)$$

$$\mathrm{pH} = 14 + \log[\mathrm{OH}^{-}] + \log\gamma \qquad (3)$$

The potentials were further corrected by subtracting the product of the measured current (i) and the uncompensated resistance obtained from EIS (R_U) according to **Equation 4** to compensate for the ohmic potential drop due to R_U.

$$E_{corrected} = E_{RHE} - i \cdot R_U \qquad (4)$$

Conversion of glycerol was calculated according to **Equation 5,** considering the initial moles of glycerol (n_0) and the moles remaining at the moment of sampling (n_i) as determined by HPLC.

To obtain n_i, the volume of the anode reservoir, corrected by the total sample volume taken up to that moment, was considered.

$$\% \text{ conversion} = \frac{n_0 - n_i}{n_0} \cdot 100 \qquad (5)$$

The Faradaic Efficiency (%FE) towards the formation of individual GOR products (FE_p) was calculated according to **Equation 6**, taking into account the sample volume (V), the product concentration (C_p), the number of electrons transferred (n_p), the Faraday constant (F), the stoichiometric factor (s_p) and the total charge passed during the measurement (Q).[30]

$$\%FE = \frac{1}{s_p} \cdot \frac{V\, C_p\, n_p\, F}{Q} \cdot 100 \qquad (6)$$

AUTHOR INFORMATION

Corresponding Author

* E-mail: wolfgang.schuhmann@rub.de; dulce.morales_hernandez@helmholtz-berlin.de.

Present Addresses

† Present address for D. M. M.: Nachwuchsgruppe Gestaltung des Sauerstoffentwicklungsmechanismus, Helmholtz-Zentrum Berlin für Materialien und Energie GmbH, Hahn-Meitner-Platz 1, 14109 Berlin, Germany.

Author Contributions

The manuscript was written through contributions of all authors. All authors have given approval to the final version of the manuscript. ‡ These authors contributed equally.

Funding Sources

Deutsche Forschungsgemeinschaft in the framework of the Research Unit 2982 “UNODE – Unusual Anode Reactions” [433304666, 433304702].

Ministry of Science and Higher Education of the Russian Federation within the state assignment for Boreskov Institute of Catalysis (project # AAAA-A21-121011390054-1).

ASSOCIATED CONTENT

Supporting Information.

The Supporting Information is available free of charge and includes reported reaction pathways (Scheme S1), high resolution TEM images (Figure S1), summary of characterization (Table S1), XRD patterns of as-prepared catalysts (Figure S2), XPS spectra (Figure S3), an example of determination of double layer capacitance (Figure S4), summary of double layer capacitance measurements (Table S2), comparison between catalytic activity, surface area and double layer capacitance (Figure S5), OER and GOR activity of MWCNTs-Ox (Figure S6), an example of product assignment in a HPLC chromatogram (Figure S7), Faradaic efficiency profiles (Figure S8), product analysis by ^{13}C-NMR (Figure S9), and XRD patterns before and after electrolysis (Figure S10).

ACKNOWLEDGMENTS

We are grateful to M. Gartmann, NMR Core Facility, Faculty of Chemistry and Biochemistry, Ruhr University Bochum, for support with the pulse sequences for NMR measurements, and to João R. C. Junqueira for the initial design of the flow-through electrolyzer. The Deutsche Forschungsgemeinschaft is acknowledged for funding in the framework of the Research Unit 2982 “UNODE – Unusual Anode Reactions” [433304666, 433304702].” M. A. K. acknowledges the support of the Ministry of Science and Higher Education of the Russian Federation within the state assignment for Boreskov Institute of Catalysis (project # AAAA-A21-121011390054-1).

REFERENCES

(1) Song, J.; Wei, C.; Huang, Z.-F.; Liu, C.; Zeng, L.; Wang, X.; Xu, Z. J. A review on fundamentals for designing oxygen evolution electrocatalysts. *Chem. Soc. Rev.* **2020**, *49* (7), 2196–2214. DOI: 10.1039/C9CS00607A.

(2) Shi, Q.; Zhu, C.; Du, D.; Lin, Y. Robust noble metal-based electrocatalysts for oxygen evolution reaction. *Chem. Soc. Rev.* **2019**, *48* (12), 3181–3192. DOI: 10.1039/c8cs00671g.

(3) Galán-Mascarós, J. R. Water oxidation at electrodes modified with earth-abundant transition-metal catalysts. *ChemElectroChem* **2015**, *2* (1), 37–50. DOI: 10.1002/celc.201402268.

(4) Jiao, Y.; Zheng, Y.; Jaroniec, M.; Qiao, S.-Z. Design of electrocatalysts for oxygen- and hydrogen-involving energy conversion reactions. *Chem. Soc. Rev.* **2015**, *44* (8), 2060–2086. DOI: 10.1039/c4cs00470a.

(5) Pittkowski, R.; Krtil, P.; Rossmeisl, J. Rationality in the new oxygen evolution catalyst development. *Curr. Opin. Electrochem.* **2018**, *12*, 218–224. DOI: 10.1016/j.coelec.2018.11.014.

(6) Zeng, K.; Zheng, X.; Li, C.; Yan, J.; Tian, J.-H.; Jin, C.; Strasser, P.; Yang, R. Recent advances in non-noble bifunctional oxygen electrocatalysts toward large-scale production. *Adv. Funct. Mater.* **2020**, *30* (27), 2000503. DOI: 10.1002/adfm.202000503.

(7) Bender, M. T.; Yuan, X.; Choi, K.-S. Alcohol oxidation as alternative anode reactions paired with (photo)electrochemical fuel production reactions. *Nat. Commun.* **2020**, *11* (1), 4594. DOI: 10.1038/s41467-020-18461-1.

(8) Xu, Y.; Zhang, B. Recent advances in electrochemical hydrogen production from water assisted by alternative oxidation reactions. *ChemElectroChem* **2019**, *6* (13), 3214–3226. DOI: 10.1002/celc.201900675.

(9) Lamy, C.; Jaubert, T.; Baranton, S.; Coutanceau, C. Clean hydrogen generation through the electrocatalytic oxidation of ethanol in a Proton Exchange Membrane Electrolysis Cell (PEMEC): Effect of the nature and structure of the catalytic anode. *J. Power Sources* **2014**, *245*, 927–936. DOI: 10.1016/j.jpowsour.2013.07.028.

(10) Fei, L.; Sun, H.; Ran, R.; Zhou, W.; Shao, Z. Self-supported nickel phosphide electrode for efficient alkaline water-to-hydrogen conversion via urea electrolysis. *Ind. Eng. Chem. Res.* **2021**, *60* (3), 1185–1193. DOI: 10.1021/acs.iecr.0c05565.

(11) Barwe, S.; Weidner, J.; Cychy, S.; Morales, D. M.; Dieckhöfer, S.; Hiltrop, D.; Masa, J.; Muhler, M.; Schuhmann, W. Electrocatalytic oxidation of 5-(hydroxymethyl)furfural using high-surface-area nickel boride. *Angew. Chem. Int. Ed.* **2018**, *57* (35), 11460–11464. DOI: 10.1002/anie.201806298.

(12) Chen, G.-F.; Luo, Y.; Ding, L.-X.; Wang, H. Low-voltage electrolytic hydrogen production derived from efficient water and ethanol oxidation on fluorine-modified FeOOH anode. *ACS Catal.* **2018**, *8* (1), 526–530. DOI: 10.1021/acscatal.7b03319.

(13) Garlyyev, B.; Xue, S.; Fichtner, J.; Bandarenka, A. S.; Andronescu, C. Prospects of value-added chemicals and hydrogen via electrolysis. *ChemSusChem* **2020**, *13* (10), 2513–2521. DOI: 10.1002/cssc.202000339.

(14) Zhou, Y.; Shen, Y.; Piao, J. Sustainable conversion of glycerol into value-added chemicals by selective electro-oxidation on Pt-based catalysts. *ChemElectroChem* **2018**, *5* (13), 1636–1643. DOI: 10.1002/celc.201800309.

(15) Cha, H. G.; Choi, K.-S. Combined biomass valorization and hydrogen production in a photoelectrochemical cell. *Nat. Chem.* **2015**, *7* (4), 328–333. DOI: 10.1038/nchem.2194.

(16) You, B.; Liu, X.; Jiang, N.; Sun, Y. A general strategy for decoupled hydrogen production from water splitting by integrating oxidative biomass valorization. *J. Am. Chem. Soc.* **2016**, *138* (41), 13639–13646. DOI: 10.1021/jacs.6b07127.

(17) You, B.; Liu, X.; Liu, X.; Sun, Y. Efficient H_2 evolution coupled with oxidative refining of alcohols via a hierarchically porous nickel bifunctional electrocatalyst. *ACS Catal.* **2017**, *7* (7), 4564–4570. DOI: 10.1021/acscatal.7b00876.

(18) Liu, W.-J.; Dang, L.; Xu, Z.; Yu, H.-Q.; Jin, S.; Huber, G. W. Electrochemical oxidation of 5-hydroxymethylfurfural with NiFe layered double hydroxide (LDH) nanosheet catalysts. *ACS Catal.* **2018**, *8* (6), 5533–5541. DOI: 10.1021/acscatal.8b01017.

(19) Amaral, P. F. F.; Ferreira, T. F.; Fontes, G. C.; Coelho, M. A. Z. Glycerol valorization: New biotechnological routes. *Food Bioprod. Process.* **2009**, *87* (3), 179–186. DOI: 10.1016/j.fbp.2009.03.008.

(20) Dai, C.; Sun, L.; Liao, H.; Khezri, B.; Webster, R. D.; Fisher, A. C.; Xu, Z. J. Electrochemical production of lactic acid from glycerol oxidation catalyzed by AuPt nanoparticles. *J. Catal.* **2017**, *356*, 14–21. DOI: 10.1016/j.jcat.2017.10.010.

(21) Lam, C. H.; Bloomfield, A. J.; Anastas, P. T. A switchable route to valuable commodity chemicals from glycerol via electrocatalytic oxidation with an earth abundant metal oxidation catalyst. *Green Chem.* **2017**, *19* (8), 1958–1968. DOI: 10.1039/C7GC00371D.

(22) Murcia Valderrama, M. A.; van Putten, R.-J.; Gruter, G.-J. M. The potential of oxalic – and glycolic acid based polyesters (review). Towards CO_2 as a feedstock (Carbon Capture and Utilization – CCU). *Eur. Polym. J.* **2019**, *119*, 445–468. DOI: 10.1016/j.eurpolymj.2019.07.036.

(23) Sawada, H.; Murakami, T. Oxalic acid. In *Encyclopedia of Chemical Technology*; Kirk-Othmer, Ed.; John Wiley & Sons, Inc, 2000. DOI: 10.1002/0471238961.

(24) Villa, A.; Dimitratos, N.; Chan-Thaw, C. E.; Hammond, C.; Prati, L.; Hutchings, G. J. Glycerol oxidation using gold-containing catalysts. *Acc. Chem. Res.* **2015**, *48* (5), 1403–1412. DOI: 10.1021/ar500426g.

(25) Fan, L.; Liu, B.; Liu, X.; Senthilkumar, N.; Wang, G.; Wen, Z. Recent progress in electrocatalytic glycerol oxidation. *Energy Technol.* **2021**, *9* (2), 2000804. DOI: 10.1002/ente.202000804.

(26) Giertyas, C.; Silva, D.; Silva, C.; Meneghetti, M.; Meneghetti, S.; Almeida, R.; Bortoluzzi, J. Improvement of an analytical method based on HPLC with refractive index detection for the analysis of glycerol oxidation products. *Quim. Nova (Química Nova)* **2019**, *42* (7), 729–735. DOI: 10.21577/0100-4042.20170391.

(27) Oliveira, V. L.; Morais, C.; Servat, K.; Napporn, T. W.; Tremiliosi-Filho, G.; Kokoh, K. B. Studies of the reaction products resulted from glycerol electrooxidation on Ni-based materials in alkaline medium. *Electrochim. Acta* **2014**, *117*, 255–262. DOI: 10.1016/j.electacta.2013.11.127.

(28) Li, Y.; Wei, X.; Chen, L.; Shi, J.; He, M. Nickel-molybdenum nitride nanoplate electrocatalysts for concurrent electrolytic hydrogen and formate productions. *Nat. Commun.* **2019**, *10* (1), 5335. DOI: 10.1038/s41467-019-13375-z.

(29) Habibi, B.; Delnavaz, N. Electrooxidation of glycerol on nickel and nickel alloy (Ni–Cu and Ni–Co) nanoparticles in alkaline media. *RSC Adv.* **2016**, *6* (38), 31797–31806. DOI: 10.1039/C5RA26006J.

(30) Han, X.; Sheng, H.; Yu, C.; Walker, T. W.; Huber, G. W.; Qiu, J.; Jin, S. Electrocatalytic oxidation of glycerol to formic acid by $CuCo_2O_4$ spinel oxide nanostructure catalysts. *ACS Catal.* **2020**, *10* (12), 6741–6752. DOI: 10.1021/acscatal.0c01498.

(31) Bott-Neto, J. L.; Martins, T. S.; Machado, S. A. S.; Ticianelli, E. A. Electrocatalytic oxidation of methanol, ethanol, and glycerol on $Ni(OH)_2$ nanoparticles encapsulated with polyNi(salen) film. *ACS Appl. Mater. Inter.* **2019**, *11* (34), 30810–30818. DOI: 10.1021/acsami.9b08441.

(32) Houache, M. S.; Cossar, E.; Ntais, S.; Baranova, E. A. Electrochemical modification of nickel surfaces for efficient glycerol electrooxidation. *J. Power Sources* **2018**, *375*, 310–319. DOI: 10.1016/j.jpowsour.2017.08.089.

(33) Han, J.; Kim, Y.; Kim, H. W.; Jackson, D. H.; Lee, D.; Chang, H.; Chae, H.-J.; Lee, K.-Y.; Kim, H. J. Effect of atomic-layer-deposited TiO_2 on carbon-supported Ni catalysts for

electrocatalytic glycerol oxidation in alkaline media. *Electrochem. Commun.* **2017**, *83*, 46–50. DOI: 10.1016/j.elecom.2017.08.023.

(34) Houache, M. S. E.; Hughes, K.; Safari, R.; Botton, G. A.; Baranova, E. A. Modification of nickel surfaces by bismuth: Effect on electrochemical activity and selectivity toward glycerol. *ACS Appl. Mater. Inter.* **2020**, *12* (13), 15095–15107. DOI: 10.1021/acsami.9b22378.

(35) Brix, A. C.; Morales, D. M.; Braun, M.; Jambrec, D.; Junqueira, J. R. C.; Cychy, S.; Seisel, S.; Masa, J.; Muhler, M.; Andronescu, C.; Schuhmann, W. Electrocatalytic oxidation of glycerol using solid-state synthesised nickel boride: Impact of key electrolysis parameters on product selectivity. *ChemElectroChem* **2021**, *8* (12), 2336–2342. DOI: 10.1002/celc.202100739.

(36) Elumeeva, K.; Kazakova, M. A.; Morales, D. M.; Medina, D.; Selyutin, A. G.; Golubtsov, G. V.; Ivanov, Y.; Kuznetsov, V. L.; Chuvilin, A.; Antoni, H.; Muhler, M.; Schuhmann, W.; Masa, J. Bifunctional oxygen reduction/oxygen evolution activity of mixed Fe/Co oxide nanoparticles with variable Fe/Co ratios supported on multiwalled carbon nanotubes. *ChemSusChem* **2018**, *11* (7), 1204–1214. DOI: 10.1002/cssc.201702381.

(37) Kazakova, M. A.; Morales, D. M.; Andronescu, C.; Elumeeva, K.; Selyutin, A. G.; Ishchenko, A. V.; Golubtsov, G. V.; Dieckhöfer, S.; Schuhmann, W.; Masa, J. Fe/Co/Ni mixed oxide nanoparticles supported on oxidized multi-walled carbon nanotubes as electrocatalysts for the oxygen reduction and the oxygen evolution reactions in alkaline media. *Catal. Today* **2020**, *357*, 259–268. DOI: 10.1016/j.cattod.2019.02.047.

(38) Morales, D. M.; Kazakova, M. A.; Dieckhöfer, S.; Selyutin, A. G.; Golubtsov, G. V.; Schuhmann, W.; Masa, J. Trimetallic Mn-Fe-Ni oxide nanoparticles supported on multi-walled

carbon nanotubes as high-performance bifunctional ORR/OER electrocatalyst in alkaline media. *Adv. Funct. Mater.* **2020**, *30* (6), 1905992. DOI: 10.1002/adfm.201905992.

(39) Morales, D. M.; Kazakova, M. A.; Purcel, M.; Masa, J.; Schuhmann, W. The sum is more than its parts: stability of MnFe oxide nanoparticles supported on oxygen-functionalized multi-walled carbon nanotubes at alternating oxygen reduction reaction and oxygen evolution reaction conditions. *J. Solid State Electrochem.* **2020**, *50* (94), 14760. DOI: 10.1007/s10008-020-04667-2.

(40) Subbaraman, R.; Tripkovic, D.; Chang, K.-C.; Strmcnik, D.; Paulikas, A. P.; Hirunsit, P.; Chan, M.; Greeley, J.; Stamenkovic, V. R.; Markovic, N. M. Trends in activity for the water electrolyser reactions on 3*d* M(Ni,Co,Fe,Mn) hydr(oxy)oxide catalysts. *Nat. Mater.* **2012**, *11* (6), 550–557. DOI: 10.1038/nmat3313.

(41) Bockris, J. O.; Otagawa, T. The Electrocatalysis of Oxygen Evolution on Perovskites. *J. Electrochem. Soc.* **1984**, *131* (2), 290–302. DOI: 10.1149/1.2115565.

(42) Kazakova, M. A.; Selyutin, A. G.; Ishchenko, A. V.; Lisitsyn, A. S.; Koltunov, K. Y.; Sobolev, V. I. Co/multi-walled carbon nanotubes as highly efficient catalytic nanoreactor for hydrogen production from formic acid. *Int. J. Hydrogen Energ.* **2020**, *45* (38), 19420–19430. DOI: 10.1016/j.ijhydene.2020.05.127.

(43) Kazakova, M. A.; Andreev, A. S.; Selyutin, A. G.; Ishchenko, A. V.; Shuvaev, A. V.; Kuznetsov, V. L.; Lapina, O. B.; d'Espinose de Lacaillerie, J.-B. Co metal nanoparticles deposition inside or outside multi-walled carbon nanotubes via facile support pretreatment. *Appl. Surf. Sci.* **2018**, *456*, 657–665. DOI: 10.1016/j.apsusc.2018.06.124.

(44) Morales, D. M.; Risch, M. Seven steps to reliable cyclic voltammetry measurements for the determination of double layer capacitance. *J. Phys. Energy* **2021**, *3* (3), 34013. DOI: 10.1088/2515-7655/abee33.

(45) Heese-Gärtlein, J.; Morales, D. M.; Rabe, A.; Bredow, T.; Schuhmann, W.; Behrens, M. Factors governing the activity of a-MnO_2 catalysts in the oxygen evolution reaction: conductivity vs. exposed surface area of cryptomelane. *Chem. Eur. J.* **2020.** DOI: 10.1002/chem.201905090.

(46) Wang, Y.; Li, J.; Wei, Z. Transition-metal-oxide-based catalysts for the oxygen reduction reaction. *J. Mater. Chem. A* **2018**, *6* (18), 8194–8209. DOI: 10.1039/C8TA01321G.

(47) Antolini, E. Glycerol electro-oxidation in alkaline media and alkaline direct glycerol fuel cells. *Catalysts* **2019**, *9* (12), 980. DOI: 10.3390/catal9120980.

(48) Tao, H. B.; Xu, Y.; Huang, X.; Chen, J.; Pei, L.; Zhang, J.; Chen, J. G.; Liu, B. A general method to probe oxygen evolution intermediates at operating conditions. *Joule* **2019**, *3* (6), 1498–1509. DOI: 10.1016/j.joule.2019.03.012.

(49) El-Shafei, A. A. Electrocatalytic oxidation of methanol at a nickel hydroxide/glassy carbon modified electrode in alkaline medium. *J. Electroanal. Chem.* **1999**, *471* (2), 89–95. DOI: 10.1016/S0022-0728(99)00235-1.

(50) Barbosa, A.; Oliveira, V. L.; van Drunen, J.; Tremiliosi-Filho, G. Ethanol electro-oxidation reaction using a polycrystalline nickel electrode in alkaline media: Temperature influence and reaction mechanism. *J. Electroanal. Chem.* **2015**, *746*, 31–38. DOI: 10.1016/j.jelechem.2015.03.024.

(51) Casella, I. G.; Cataldi, T. R. I.; Salvi, A. M.; Desimoni, E. Electrocatalytic oxidation and liquid chromatographic detection of aliphatic alcohols at a nickel-based glassy carbon modified electrode. *Anal. Chem.* **1993**, *65* (21), 3143–3150. DOI: 10.1021/ac00069a032.

(52) Zeng, K.; Zhang, D. Recent progress in alkaline water electrolysis for hydrogen production and applications. *Prog. Energy Combust. Sci.* **2010**, *36* (3), 307–326. DOI: 10.1016/j.pecs.2009.11.002.

(53) Nguyen, R.; Amouroux, M.; Duda, A.; Mouloungui, Z. Quantification of mixtures of C2 and C3 hydroxy acids and products of glycerol oxidation by high-performance liquid chromatography and quantitative ^{13}C NMR. *J. Am. Oil Chem. Soc.* **2020**, *97* (7), 679–689. DOI: 10.1002/aocs.12349.

(54) Andreev, A. S.; Krasnikov, D. V.; Zaikovskii, V. I.; Cherepanova, S. V.; Kazakova, M. A.; Lapina, O. B.; Kuznetsov, V. L.; d'Espinose de Lacaillerie, J.-B. Internal field 59Co NMR study of cobalt-iron nanoparticles during the activation of $CoFe_2$/CaO catalyst for carbon nanotube synthesis. *J. Catal.* **2018**, *358*, 62–70. DOI: 10.1016/j.jcat.2017.11.025.

(55) Golubtsov, G. V.; Kazakova, M. A.; Selyutin, A. G.; Ishchenko, A. V.; Kuznetsov, V. L. Mono-, bi-, and trimetallic catalysts for the synthesis of multiwalled carbon nanotubes based on iron subgroup metals. *J. Struct. Chem.* **2020**, *61* (4), 640–651. DOI: 10.1134/S0022476620040186.

(56) Kuznetsov, V. L.; Elumeeva, K.; Ishchenko, A. V.; Beylina, N. Y.; Stepashkin, A. A.; Moseenkov, S. I.; Plyasova, L. M.; Molina, I. Y.; Romanenko, A. I.; Anikeeva, O. B.; Tkachev,

E. N. Multi-walled carbon nanotubes with ppm level of impurities. *Phys. Status Solidi B* **2010**, *247* (11-12), 2695–2699. DOI: 10.1002/pssb.201000211.

(57) Wuttig, A.; Surendranath, Y. Impurity ion complexation enhances carbon dioxide reduction catalysis. *ACS Catal.* **2015**, *5* (7), 4479–4484. DOI: 10.1021/acscatal.5b00808.

(58) Bromley, L. A. Thermodynamic properties of strong electrolytes in aqueous solutions. *AIChE J.* **1973**, *19* (2), 313–320. DOI: 10.1002/aic.690190216.

(59) Knobel, M. The activities of the ions of potassium hydroxide in aqueous solution. *J. Am. Chem. Soc.* **1923**, *45* (1), 70–76. DOI: 10.1021/ja01654a010.

(60) Balej, J. Activity coefficients of aqueous solutions of NaOH and KOH in wide concentration and temperature ranges. *Collect. Czech. Chem. Commun.* **1996**, *61* (11), 1549–1562. DOI: 10.1135/cccc19961549.

TABLE OF CONTENTS